

Sum frequency generation surface spectra of ice, water, and acid solution investigated by an exciton model

V. Buch^{a)}*The Fritz Haber Institute for Molecular Dynamics, The Hebrew University, Jerusalem 91904, Israel*

T. Tarbuck and G. L. Richmond

Department of Chemistry, University of Oregon, Eugene, Oregon 97403, USA

H. Groenzin, I. Li, and M. J. Shultz

Department of Chemistry, Tufts University, Medford, Massachusetts 02155, USA

(Received 4 June 2007; accepted 5 September 2007; published online 28 November 2007)

A new computational scheme is presented for calculation of sum frequency generation (SFG) spectra, based on the exciton model for OH bonds. The scheme is applied to unified analysis of the SFG spectra in the OH-stretch region of the surfaces of ice, liquid water, and acid solution. A significant role of intermolecularly coupled collective modes is pointed out. SFG intensity amplification observed for acid solutions in the H-bonded OH-stretch region is reproduced qualitatively and accounted for by enhanced orientational preference “into the surface” of the H₂O bisectors within the hydronium solvation shell. © 2007 American Institute of Physics. [DOI: 10.1063/1.2790437]

I. INTRODUCTION

The sum frequency generation (SFG) technique emerged as a valuable tool for studying interfaces, due to surface specificity of this spectroscopic technique. The interface of liquid water, aqueous solutions, and ice with air received particular attention due to the importance of H₂O in nature and in the laboratory; see, e.g., Refs. 1–10. The SFG spectra of liquid H₂O include a peak at 3700 cm⁻¹, assigned to dangling OH, and a broad H-bonded band at lower frequencies; the latter band, which is the main topic of the present study, probes the H bonding within the surface layer. Interpretation of the H-bonded band has been a subject of considerable discussion; its low and high frequency parts were assigned to an “icelike” and a disordered component of water, respectively;¹ assignments were also proposed based on different coordinations and solvation shell configurations of water molecules.^{9,10}

In parallel to the SFG investigations, much computational research has been devoted recently to surfaces of aqueous solutions, following the realization that the surface composition and chemistry are quite unique and may differ considerably from that of the bulk;^{11,12} moreover chemistry at aqueous interfaces is likely to play an important role in atmospheric chemistry (see, e.g., Refs. 13–16). One of the striking recent findings has been computational demonstration of the preference of protonated water for surface sites.^{6,17,18} This finding is consistent with experimental observation of SFG signal enhancement in the H-bonded OH-stretch region for acid solutions with respect to neat water.^{2,6,19–21} Other evidence indicating surface preference of protonated water includes computational and spectroscopic

studies of large protonated-water clusters^{22–25} and second harmonic generation experiments on solutions.²⁶

Advances in SFG investigations motivated development of computational techniques to bridge between molecular level simulations of aqueous surfaces and measured SFG spectra; the ultimate goal being microscopic interpretation of the observed spectral line shapes. The basic SFG formalism has been discussed and summarized in a number of published studies, see, e.g., Refs. 1 and 27–32. Practical applications to OH-stretch spectrum of aqueous systems are non-trivial, considering that a coupled anharmonic many body system is considered and that molecular vibrations of interest do not satisfy the classical limit (i.e., $\hbar\omega \ll k_B T$). Another computational problem is scarcity of accurate *flexible* potentials and of empirical functions describing system dipole and polarizability as a function of molecular configuration; the latter quantities are needed to evaluate the SFG spectra. Nevertheless, considerable progress has been made in modeling of the surface spectrum of neat water^{33–37} and of an aqueous salt solution.^{38,39} Nearly all these studies employ the time correlation function formalism.^{34–37} Classical molecular dynamics is used to evaluate the quantum-corrected cross-correlation function between the system dipole and the polarizability. An exception is Ref. 33, in which a quantum treatment of OH-stretch vibrations was presented; however, some of the assumptions of this initial model (SFG signal taken as a sum of contributions of individual water molecules and neglect of intermolecular coupling) were later shown to be problematic.³⁷ In Ref. 9, the model of Ref. 33 was expanded to include intermolecular coupling between near-neighbor H-bonded molecules.

In the present study, a quantum-mechanical treatment is presented for SFG spectra of H₂O in the OH-stretch region, which includes long range intermolecular coupling and which allows for convenient qualitative interpretation of the

^{a)}Electronic mail: viki@fh.huji.ac.il

spectra. The treatment is based on the exciton model. That is, a vibrational excitation is viewed as a linear combination of excitations delocalized over the different OH bonds within the system. The different OH-bond vibrations are coupled by intramolecular and intermolecular (dipole-dipole) coupling; thus, a possibility of excitations extending over numerous OH bonds is automatically included in the model. In addition, the model incorporates the well-known dependence of the OH-bond frequency on the strength of the local hydrogen bonding. This exciton model was used by us in the past for the analysis of the infrared (IR) and Raman spectra of ice,⁴⁰ ice surfaces,⁴¹ ice nanocrystals,⁴² water clusters,^{43,44} and liquid H₂O.⁴⁵ Our scheme incorporates elements of preceding computational work by the groups of Rice *et al.*⁴⁶ and Reimers and Watts *et al.*⁴⁷ A related model has been recently employed by Corcelli *et al.*⁴⁸ to analyze ultrafast infrared spectroscopy of dilute HOD in liquid water, and infrared and Raman line shapes of dilute HOD as a function of temperature.⁴⁹

Here, an extension of the exciton model is presented to the SFG spectra. Inclusion of intermolecular coupling is crucial for treatment of ice since, as shown in the past, OH-stretch excitations are delocalized over the ice sample.⁴⁰ The presence of extended OH modes in liquid water was proposed in the past based on the analysis of IR and Raman spectra,^{46,50–52} and supported by recent calculations by ourselves⁴⁵ and others.⁵³ The need to include intermolecular correlations was also noted in recent computational studies of SFG spectra of aqueous surfaces, employing classical time cross-correlation functions.³⁷

The present computational scheme is applied to the analysis of experimental SFG spectra of surfaces of ice, neat liquid water, and aqueous acid solution. For comparison with ice calculations, new experimental spectra are used which were obtained in the Shultz laboratory for single crystal ice surfaces.⁸ For comparison with calculations for the liquid phase, data from the Richmond laboratory are employed pertaining to isotopic dilution studies⁵⁴ as well as to acid solvation effects.²¹ Computations of the dependence of SFG-*ppp* spectra on the visible light incidence angle, for neat liquid H₂O, are tested against experimental data obtained by Gan *et al.*¹⁰

In Sec. II of the article, the computational scheme is described. In Sec. III, the results for ice are discussed. Section IV addresses liquid spectra. Section V focuses on a simulation with a hydronium ion at the liquid surface. The results are summarized in Sec. VI.

II. THE COMPUTATIONAL SCHEME

The basic exciton model, which was used in the past to study IR and Raman spectra of H₂O, is described in Refs. 42, 44, and 45. Here, a version described in Ref. 45 is extended to include SFG spectra. The scheme is summarized briefly below.

OH bonds are treated as coupled local Morse oscillators. Vibrationally excited states describing OH-stretch motion are expanded in the exciton basis, $\psi_{\text{exc}} = \sum_b c_b |1_b\rangle$, where $|1_b\rangle$ is a product basis state with one quantum in bond b and zero

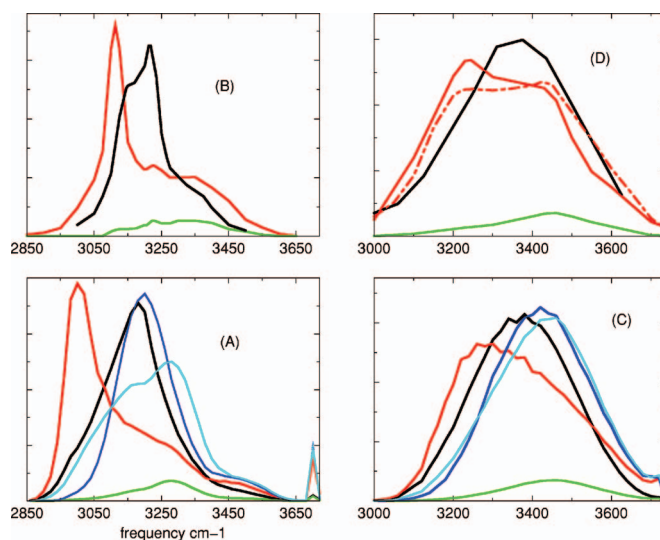


FIG. 1. (Color) Spectra of H₂O ice (left panels) and of liquid water (right panels). Color coding: black, IR; red, parallel-polarized Raman (the incoming polarization parallel to the outgoing polarization, spectrum averaged over all possible incoming polarizations); green, perpendicular-polarized Raman (the incoming polarization perpendicular to the outgoing polarization, averaged over all possible polarization directions); blue, density of bond frequencies; and cyan, density of states. Relative units; parallel and perpendicular-polarized Raman are on the same scale. (A) Computed spectra of top five bilayers (300 molecules) of an ice slab at 190 K. (B) Experimental ice spectra, Raman spectra are averages over different polarizations of 167 K single crystal spectra given in Ref. 63. IR spectrum at 150 K from Ref. 46. (C) Calculated liquid spectra for top 300 molecules of a liquid slab at 275 K. (D) Experimental liquid spectra. Polarized Raman spectra derived from isotropic and anisotropic spectra of Ref. 64 at 263 K (solid) and 283 K (dashed). IR spectra at 298 K adopted from Ref. 65.

quanta in the remaining bonds. The sum is over the different OH bonds within the system. The vibrational ground state is modeled as a product state corresponding to zero quanta in each bond.

The OH bonds are coupled via intra- and intermolecular coupling; the latter is modeled as an oscillating dipole-dipole interaction. Note that in condensed phases the intramolecular coupling is much smaller than in the gas phase; as can be inferred from the modest symmetric-asymmetric stretch splitting of H₂O in the water octamer:⁴⁴ 24–30 cm⁻¹, as compared to 110 cm⁻¹ for gaseous H₂O. A similarly small splitting of 45 cm⁻¹ was measured for H₂O molecules isolated in D₂O ice.⁵⁵ The reason for the small splitting in ice and clusters is cancellation between intramolecular OH..OH potential coupling and the momentum coupling which is due to the shared O atom, while in the gas the potential coupling constant has a different sign and the two terms add up.⁴⁴

On the other hand, the bond dipole derivative increases substantially upon hydrogen bonding,^{42,48,56} resulting in substantial intermolecular coupling between OH vibrations, especially between the ones corresponding to strongly H-bonded OH. Moreover the dipole-dipole interaction is long ranged. As a result, vibrational excitations in ice are delocalized over the tetrahedral H-bond network. (Clear experimental evidence for such delocalization comes, e.g., from the fact that IR, parallel-polarized Raman, and perpendicular-polarized Raman line shapes of ice are different from each other, see Fig. 1; this is since the different

spectra correspond to preferential excitation of different collective OH modes.) The parameters for intra- and intermolecular coupling are given in Ref. 42.

The influence of H bonding on OH stretch is modeled by assuming that the OH-bond frequency is a decreasing function $\omega(E)$, where E denotes the electric field component parallel to OH at the H atom. E is calculated as the field of the fixed charges and the induced dipoles of an empirical polarizable potential (EMP).^{57,58} The function $\omega(E)$ was calibrated against spectra of water clusters. As in the past studies,^{44,45,59} the coupling between inter- and intramolecular motions was modeled via averaging the electric field E over intermolecular motion. Essentially, thermal excitation displaces OH bonds from the local minimum energy locations, thus weakening the H bonds and reducing the size of the OH-stretch frequency redshifts which are due to the H bonding. In reality, the distribution of intermolecular configurations has contributions both from zero-point delocalization and from thermal excitations. However, in the present study intermolecular motion is treated classically and the mean E value is obtained via averaging over sections of classical trajectories. Such averaging is used to represent the temperature effect on the spectra. Note that in the classical trajectories the molecules are treated as rigid, in the framework of the SHAKE algorithm.⁶⁰ The mean E values are calculated from classical molecular dynamics (MD) and used subsequently to construct the quantum-mechanical OH-stretch Hamiltonian matrix for a given section of a trajectory.

In the case of ice, calculation of spectra requires additional averaging over the possible orientational configurations. The normal hexagonal ice is “proton disordered,” i.e., only the oxygens form a periodic pattern, while molecular orientations are random within the constraint of completeness of the tetrahedral hydrogen bond network.⁶¹ In the ice solid, transitions between different orientational structures occur via passage of orientational defects, on a time scale which is way too long for direct modeling by molecular dynamics.^{55,61} Here, ice spectra were calculated as an average over 126 different proton-disordered ice structures. The structures were constructed as described in Ref. 57, for a ten bilayer ice slab containing 600 water molecules, with two-dimensional periodic boundaries in the x , y directions; the z axis is assumed perpendicular to the open slab surfaces. The dimension of the slab was $22.7 \times 23.6 \times 37.1 \text{ \AA}^3$. The two exposed surfaces corresponded to the hexagonal basal planes. For each ice model, a 3 ps classical trajectory was run. The last 1 ps was used to obtain the average electric field E at the H atom for each OH bond, the corresponding bond frequency $\omega(E_b)$, and the average dipole-dipole coupling with other bonds. A specified number of ice bilayers (in the range 1–5) were included in the calculation of the excited OH states, on one side of the slab (the two sides contribute to the SFG signal with opposite signs;³⁶ the two contributions were calculated separately). Thus constructed Hamiltonian matrix for the OH-stretch excitations of dimension $2N \times 2N$ (N denotes the number of included H_2O) was diagonalized to obtain the vibrationally excited states. These states were then used to evaluate SFG spectra.

For the studies of the liquid surface, one of the above ice

slab models was melted, and an extended classical trajectory was computed to generate input structures for spectra calculations. The trajectory was run at 275 K, about 30 K above the slab melting point for the EMP. (There is an inherent uncertainty in the temperature which should be used to model room temperature liquid properties; the question is whether one should use 298 K or a temperature defined with respect to the melting point of a given potential. Fortunately, the temperature dependence of both the computed and the measured SFG spectra of liquid water is modest.⁶² Low liquid temperature was chosen for the simulations to facilitate comparison with ice results.)

In the case of the liquid spectra, continuous evolution of the hydrogen bond network must be taken into account. One might consider an adiabatic approximation in which the spectra are calculated for a thermal distribution of instantaneous intermolecular configurations of the liquid, obtained in MD. However, past studies by other authors^{46,66} and our own numerical tests indicate that thus-obtained spectra are too broad; that is, the intramolecular OH vibrations “feel” a potential which is averaged to some extent over fast intermolecular motions within an inherent structure (“motional narrowing”). In the present study, the treatment was adopted from Ref. 45, where liquid IR and Raman spectra were calculated. The electric field at each OH was averaged over sections of trajectory of 1 ps duration, on the order of a lifetime of the hydrogen-bond network in liquid water; the corresponding OH Hamiltonian was constructed for this section of a trajectory, similar to ice, and diagonalized to obtain a set of excited states. SFG spectrum was calculated as a sum of contributions from several hundreds of such sets of states, obtained for different liquid H-bond configurations. The configurations were collected from a 2000 ps long classical trajectory at 3 or 4 ps intervals; alternating sides of the slab were used in the spectrum calculation to reduce structural correlations. (The 2000 ps production run was preceded by a 770 ps trajectory to ensure equilibration; the mean translational and rotational temperatures differed by about 1 K due to use of a 9 Å potential cutoff.)

Thus the liquid SFG spectrum is obtained as a mean of quasistatic contributions from a collection of snapshots of the H-bond network, averaged over local oscillations for 1 ps. A more advanced treatment would include continuous evolution of the OH states in response to changes of the H-bond network. Nevertheless, the present approximate treatment yields reasonable qualitative agreement to experiment for IR, parallel-polarized, and perpendicular-polarized Raman spectra for both ice and liquid, as seen in Fig. 1. For the formulas to calculate IR and Raman intensities for the excited states, see Refs. 41, 42, and 45.

Computation of SFG intensities is now considered. In SFG spectroscopy, the interface is irradiated by two overlapping beams, one of fixed visible frequency ω_{vis} and the other of tunable IR frequency ω . Light is emitted at the sum frequency $\omega_{\text{SF}} = \omega + \omega_{\text{vis}} \approx \omega_{\text{vis}}$. The intensity of the emitted light undergoes resonant enhancement when ω coincides with a vibrational mode of the surface. The technique is surface specific for a centrosymmetric bulk phase. The SFG intensity is proportional to^{1,27–32}

$$\omega^2 \sec^2 \beta_{\text{SF}} |\chi_{\text{eff}}^{(2)}|^2,$$

where β_{SF} denotes the reflection angle which is determined by the phase-matching condition. The second-order nonlinear susceptibility $\chi_{\text{eff}}^{(2)}$ depends on the respective polarizations of the three beams. For the *ssp* and *ppp* polarizations considered in this study,

$$\chi_{\text{eff,ssp}}^{(2)} = A \chi_{\text{yyz}},$$

$$\chi_{\text{eff,ppp}}^{(2)} = B \chi_{\text{xxz}} + C \chi_{\text{zzz}}.$$

In the above, the x and y axes are assumed, respectively, parallel and perpendicular to the plane which includes the three beams (visible, IR, and sum frequency). The coefficients A , B , C depend on the experimental system geometry and on indices of refraction of the respective media (vacuum, interface, and bulk); the expressions can be found, e.g., in Ref. 29. χ_{ijk} , $i, j, k = x, y, z$ are elements of the susceptibility tensor, which depend on properties of the material. For ice and water, matrix elements other than χ_{zzz} and $\chi_{\text{yyz}} = \chi_{\text{xxz}}$ are either zero or small, and were neglected in the above formulas.

In calculations of the SFG spectra, the χ_{ijk} elements are commonly evaluated as sums of contributions of individual molecules. However, for OH-stretch vibrations in H_2O , the effects of intermolecular coupling are significant, and one must take into account relative phases of oscillations of the different OH bonds in collective excitations. In calculations of the pertinent χ_{ijk} elements which incorporate intermolecular coupling, the formulas were adopted from the literature,^{1,27-32} while treating the entire system as one large space-fixed “molecule.”

The matrix elements relevant to the resonant contribution to χ_{ijk} are products of elements of the dipole and the polarizability derivatives. In a real macroscopic system, the $\chi_{ijk,R}$ elements are continuous functions of ω . In our limited dimensionality model we divided the entire OH-stretch spectral range 2850–3750 cm^{-1} into 45 frequency bands of width 20 cm^{-1} . $\chi_{ijk,R}$ was then obtained as

$$\langle \chi_{ijk,R} \rangle = \left\langle \sum_{\text{exc}} \langle 0 | \alpha_{ij} | \psi_{\text{exc}} \rangle \langle 0 | \mu_k | \psi_{\text{exc}} \rangle \right\rangle_{\text{av}}.$$

The sum is over all excited states within a given frequency band, for each set of states corresponding to some H-bond network configuration. The average is over all sets of states included in the calculation. α_{ij} and μ_k denote the system polarizability and dipole components, evaluated by summing over all OH-bond contributions to a given excited state.^{42,46,67} For ice, the averaging was carried out over 252 distinct surface models. (For the 126 different proton-disordered ice slab models, each of the two open surfaces was used consecutively to generate a separate set of excited states.) It was found that a minimum of ~ 70 surface configurations (corresponding to different orientational arrangements consistent with intact tetrahedral bond network⁶¹) was necessary to obtain a line shape approximating the final result. For the liquid, the convergence of the spectra with the number of configurations was slower than in the case of ice; averaging over at least ~ 250 configurations was needed.

The individual matrix elements connecting the ground state and one of the excited states were evaluated using bond dipole and bond polarizability models:^{46,67}

$$\langle 0 | \mu_k | \psi_{\text{exc}} \rangle = \sum_b c_b \mu'_b \langle 0 | \delta r_b | 1 \rangle \cos \theta_{bk}.$$

The Morse matrix element of the bond displacement $\langle 0 | \delta r_b | 1 \rangle$ is analytical.⁶⁸ The bond dipole derivative μ'_b increases with the strength of the hydrogen bond, as described in Ref. 42. θ_{bk} denotes the angle between a OH bond and the k th Cartesian axis ($\cos \theta_{bk}$ is averaged over a 1 ps long section of a classical trajectory).

The polarizability matrix element is given (in relative units) by^{46,67}

$$\langle 0 | \alpha_{i \neq j} | \psi_{\text{exc}} \rangle = \sum_b c_b a \langle 0 | \delta r_b | 1 \rangle \cos \theta_{bi} \cos \theta_{bj},$$

$$\langle 0 | \alpha_{ii} | \psi_{\text{exc}} \rangle = \sum_b c_b \langle 0 | \delta r_b | 1 \rangle (1 + a \cos^2 \theta_{bi}).$$

The a constant in the equation is given by $a = \alpha_{\parallel} / \alpha_{\perp} - 1$, where α_{\parallel} and α_{\perp} denote the bond polarizability derivatives in the directions parallel and perpendicular to the bond, respectively. The ratio $\alpha_{\parallel} / \alpha_{\perp}$ derived in the past from the analysis of Raman spectra of ice was in the range 4.5–7.0; the value recommended in Ref. 69 is 4.6. (This value was also suggested to be consistent with Raman spectra of the liquid.^{64,69}) However, this value was derived using a different (harmonic) model for H_2O . We found that a much better overall agreement with the surface SFG spectra was obtained using the value of 3.4, which is closer to 3.1 ratio derived from gas phase Raman data for H_2O .⁷⁰ Moreover the $(\alpha_{\parallel} / \alpha_{\perp}) = 3.4$ ratio yielded reasonable agreement between the computed and the experimental parallel- and perpendicular-polarized Raman spectra for bulk ice and bulk water (see Fig. 1). The computed ratio between the integrated perpendicular-polarized and parallel-polarized intensities was 0.073 (0.124) for water and was 0.099 (0.096) for ice, using the 3.4 (4.6) bond polarizability ratios; the ratio estimated from digitized experimental data is 0.10 for water and is 0.11 for ice. The ratio $\alpha_{\parallel} / \alpha_{\perp} = 3.4$ was then adopted for all OH bonds in liquid H_2O and ice. In reality, α_{\parallel} and α_{\perp} values may depend on the hydrogen bond configuration of the water molecule;^{35,36,49} the issue merits further detailed investigation.

The χ_{ijk} elements needed to obtain the SFG intensity were finally calculated as

$$\chi_{ijk}(\omega) = \chi_{ijk,\text{NR}} + \chi_{ijk,R} = \chi_{ijk,\text{NR}} + \sum_q \frac{\langle \chi_{ijk,R}(\omega_q) \rangle}{(\omega_{\text{IR}} - \omega_q + i\Gamma_q)},$$

where the sum is over all 45 bands of frequencies in the OH-stretch spectral range (2850–3740 cm^{-1}). $\langle \chi_{ijk,R}(\omega_q) \rangle$ is the resonant susceptibility element averaged over all sets of states as described above, ω_q is the center frequency of the band, Γ_q is the damping constant, and $\chi_{ijk,\text{NR}}$ is the nonresonant contribution.

At the present stage, no effort was made to derive $\chi_{ijk,\text{NR}}$ and Γ_q from first principles; they were assigned constant val-

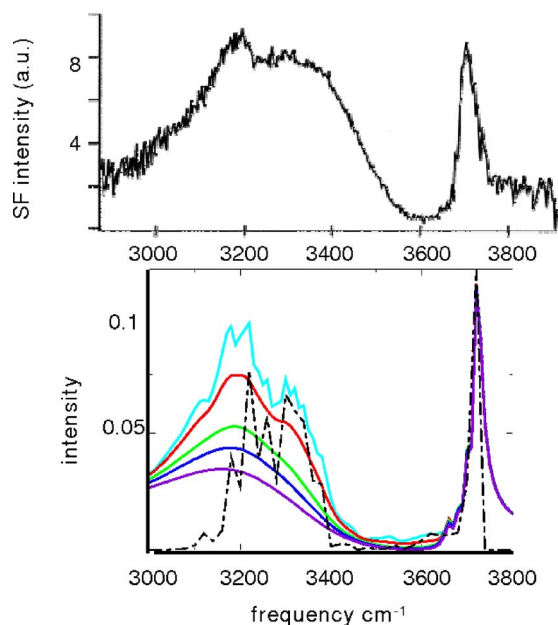


FIG. 2. (Color online) Bottom: SFG-*ssp* spectra of liquid H₂O surface, computed with different values of the damping constant Γ . Solid lines, from top to bottom: $\Gamma=15, 30, 60, 80,$ and 110 cm^{-1} at $\omega < 3650\text{ cm}^{-1}$. Above 3650 cm^{-1} (dangling-OH region), Γ was set to 10 cm^{-1} for all curves. Relative units. In all the calculations, $\chi_{\text{yyz, NR}}$ was set to 0.1 units. Dot-dashed line: $|\chi_{\text{yyz, NR}}|^2$ as a function of frequency. Five liquid layers (i.e., top 300 molecules) were included in the calculation. Top panel: experimental spectrum from Ref. 54.

ues which yield reasonable agreement with the neat liquid H₂O spectrum (Fig. 2) and used throughout the article for both liquid and ice. $\chi_{ijk, \text{NR}}$ was set to a real constant. The size of $\chi_{\text{yyz, NR}}$ determines the relative spectral intensity at the low frequency end $\sim 3000\text{ cm}^{-1}$ of the spectrum versus the “dip” at $\sim 3600\text{ cm}^{-1}$, see Fig. 2. A value of $\chi_{\text{zzz, NR}}$ which is larger by a factor of 1.3 was determined to obtain best overall agreement to the liquid *ppp* spectra (which are discussed in Sec. IV).

The inverse width h/Γ_q should be of order of relaxation time of OH-stretch excitations within the system. Recent experimental studies⁷¹ of ultrafast vibrational dynamics in liquid H₂O indicate two relaxation time scales of transient spectra—one sub-100 fs (of order of the intermolecular vibrational period), and another $\sim 1\text{ ps}$. While relaxation time scales of transient spectra studied in Ref. 71 do not translate directly to Γ_q values of the present computational scheme, they suggest a reasonable range of values to be explored. The first time scale suggests $\Gamma > 300\text{ cm}^{-1}$, the second $\Gamma \approx 30\text{ cm}^{-1}$. Figure 2 shows calculated line shapes for the *ssp* spectrum of liquid water, for a series of Γ values in the 15–110 cm^{-1} range. It is seen that inclusion of Lorentzian width modifies the spectra significantly with respect to the $|\chi_{\text{yyz}}|^2(\omega)$ line shape. In particular, the presence of the low frequency tail (which is in accord with experiment) is due entirely to the Lorentzian tail. The calculation with $\Gamma_q = 30\text{ cm}^{-1}$ for the H-bonded part of the spectrum seems to give the best agreement with experiment. This is since for larger Γ_q values the substructure of the H-bonded spectrum is smoothed out. This substructure is somewhat variable from experiment to experiment (e.g., compare the experi-

mental spectrum in Fig. 2 with spectra discussed in Sec. IV). However, the very presence of the substructure in the experimental spectra is generally accepted. Therefore, $\Gamma = 30\text{ cm}^{-1}$ was employed in all further liquid phase calculations in the H-bonded regime ($\omega_q < 3650\text{ cm}^{-1}$). For ice, a smaller value $\Gamma = 15\text{ cm}^{-1}$ was adopted in the H-bonded region, since the damping in the more rigid solid system is expected to be less effective (the difference with respect to ice spectra calculated with $\Gamma_q = 30\text{ cm}^{-1}$ is modest). For the narrow dangling-OH feature in ice and liquid a smaller value $\Gamma = 10\text{ cm}^{-1}$ was adopted.

As seen in Fig. 2, the main deficiency of the computed liquid SFG spectrum, with respect to the experiment, is missing intensity in the $3400\text{--}3500\text{ cm}^{-1}$ range. That is, the computed spectrum decreases rather abruptly in the $3340\text{--}3420\text{ cm}^{-1}$ range, as compared to the experimental spectrum which decays more gradually in the $3400\text{--}3600\text{ cm}^{-1}$ range. Discrepancy between computation and experiment is also observed in this spectral region for the ice surface, as discussed in the next section. The possible origins of this discrepancy will be addressed in Sec. VI.

In the acid simulation, the system included a single hydronium ion, with H₃O⁺-water interaction parameters chosen to reproduce the documented surface preference of protonated water.^{6,17–25,73,74} First, potential parameters for hydronium-water interaction used in Ref. 6 in conjunction with the polarizable POL3 (Ref. 72) potential were adopted; however, a calculation employing this interaction in conjunction with the EMP water potential did not reproduce the hydronium surface preference. [EMP was used since the $\omega(E)$ function needed in calculation of the spectra was calibrated for this water potential.] The problem was solved by adding an exponentially repulsive term between the hydronium oxygen and the water hydrogen to represent the hydrophobicity of the oxygen. With these parameters, the ion spent most of the 2500 ps trajectory at one of the slab surfaces. The current parameters for hydronium-water interaction may not be optimal and may exaggerate the hydronium surface preference; however, the typical surface configurations obtained in the trajectory—H₃O⁺ strongly bonded to water via three proton-donor bonds, with the O atom pointing out of the surface—are consistent with past investigations employing a variety of approaches—multistate empirical valence bond,¹⁸ an empirical potential,⁶ and on the fly dynamics.^{17,73,74} Note that the present study is not designed to *demonstrate* the surface preference of protonated water (this was done in other studies) but rather to examine the effect of such preference on the SFG spectra. Calculation of the SFG spectrum included only H₂O contributions, but not those of protonated water itself, which are expected to be very broad⁷⁵ and to extend well below the water OH-stretch range. Thus it is assumed that the experimentally observed SFG signal amplification upon addition of acid is due to preferential orientation of water molecules by the ion. The results discussed in Sec. V seem to support this assumption.

One may note that in reality, protonated water in solution undergoes continuous structural evolution bracketed by two limiting forms, hydronium H₃O⁺ and Zundel ion

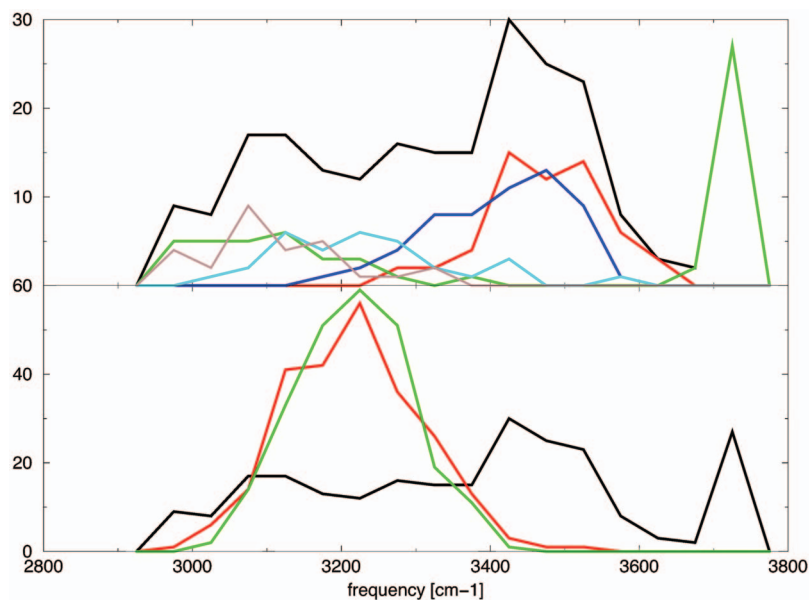


FIG. 3. (Color) Distribution of bond frequencies for one of the proton-disordered ice models. Bottom panel: black, red, and green correspond to first, second, and third ice bilayers. The top panel shows the breakdown of all top layer bond frequencies (black) to contributions originating from different coordinations. Green, three-coordinated *d*-H molecules and red, three-coordinated *d*-O. Blue and brown: OH bonds of four-coordinated molecules which are H bonded to *d*-H and *d*-O molecules, respectively. Cyan: OH bonds connecting the top bilayer to the one below.

$\text{H}_2\text{O} \cdot \cdot \text{H}^+ \cdot \cdot \text{OH}_2$.^{17,18,76–78} At the present stage of the SFG spectra calculations, the contribution of the Zundel-type configurations was not yet included.

III. RESULTS: ICE

As noted above, the exposed surface of the ice slab model is a hexagonal bilayer corresponding to the basal plane. The bilayer is puckered, with bottom half of the molecules four coordinated and top half three coordinated; each three-coordinated molecule has either a dangling-H (*d*-H) or a *d*-O atom. The surface pattern of dangling atoms varies from one proton-disordered model to another. In the ice interior, the different hydrogen bonds have similar strengths, despite the proton disorder. However, in the top bilayer the distribution of H-bond strengths and the corresponding bond-frequency distribution are considerably broader than in the interior (Fig. 3). Symmetry breaking by the surface seems to affect the H-bond strength.

The H-bonding characteristics of the top ice bilayer and the corresponding OH-bond frequencies are first discussed. As noted in past studies of ice surfaces and clusters (see, e.g., Refs. 41–43 and 79–82), *d*-O molecules form weak donor bonds and therefore correspond to relatively high bond frequencies (Fig. 3, top). On the other hand, the bonded OH of the *d*-H molecules forms strong bonds, corresponding to low OH-stretch frequencies. Moreover four-coordinated molecules in the bottom half of the top bilayer form strong donor bonds to *d*-O molecules, and weak donor bonds to *d*-H molecules. Thus 2/3 of H bonds within the top bilayer are weak, and 1/3 are strong. The vertical bonds connecting the top bilayer to the one below are also strong, corresponding to slightly higher frequencies than the strong bonds *within* the top bilayer. (See related discussion in Ref. 81 on H-bond

strengths as a function of local coordination in water clusters.)

Figure 4 shows the calculated χ elements and the SFG spectra for ice. The χ elements are first considered for decoupled OH bonds [panel (A); physically, these results correspond to HDO isotopically isolated in D_2O ice]. For the decoupled system, the matrix elements contributing to the susceptibility are still given by formulas of the previous section, with a single bond contributing to the sum (i.e., c_b equals 1 or 0) for each excited state. In the case of χ_{yyz} , bonds pointing ~ 40 deg away from the z axis yield the largest individual values of the pertinent matrix element product since the angular dependence of $\langle 0 | \alpha_{yy} | \psi_{\text{exc}} \rangle \langle 0 | \mu_z | \psi_{\text{exc}} \rangle$ is given by $(1 + a \cos^2 \theta_{by}) \cos \theta_{bz}$ (see Introduction); however, there is also a nonzero contribution from OH oriented along the z axis. Thus one may reasonably expect contributions to χ_{yyz} both from bonds within the puckered ice bilayers and from OH connecting the bilayers. The relative contributions are ultimately determined by net polarization of bonds at a given frequency. In the case of the zzz polarization, z -oriented OH yield largest matrix elements and are thus preferentially probed.

In the H-bonded region $< 3650 \text{ cm}^{-1}$, χ_{yyz} of the decoupled system includes a small negative feature at 3560 cm^{-1} , a larger positive feature at 3380 cm^{-1} , and a dominant intense negative peak at 3180 cm^{-1} . The 3560 cm^{-1} feature originates from the surface *d*-O molecules. The 3380 cm^{-1} peak originates largely from the OH bonds of the four-coordinated molecules in the top bilayer, which donate to *d*-H molecules; as noted above, the corresponding H bonds are relatively weak and correspond to relatively high frequencies. As seen in Fig. 3, the corresponding bond-frequency distribution overlaps partially with that of *d*-O molecules, resulting in destructive interference at $\sim 3480 \text{ cm}^{-1}$. The intense lowest frequency negative peak of decoupled χ_{yyz} , at 3180 cm^{-1} ,

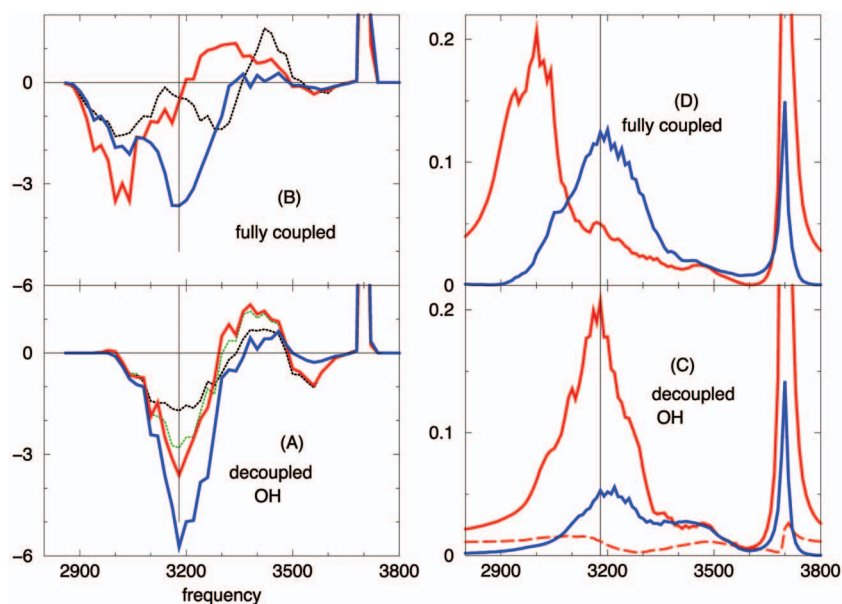


FIG. 4. (Color) Panels (A) and (B): resonant contribution to χ elements for ice; same relative units are used for all elements. Black, green, and red correspond to $\chi_{yyz} = \chi_{xz}$ calculated with one, two, and three top bilayers of ice, respectively. The results for five bilayers are very similar to those for three bilayers. Blue: χ_{zzz} , calculated with three bilayers, and reduced by a factor of 2 to ease the comparison with χ_{yyz} . (A) Decoupled OH bonds (“HDO isotopically isolated in D₂O ice”). (B) H₂O. Panels (C) and (D): computed SFG spectra; the same relative units are used for all spectra. Red, *ssp* spectrum, which is determined by χ_{yyz} , and blue, *ppp* spectrum, determined by a linear combination $B\chi_{xz} + C\chi_{zzz}$; the relative contributions ($C/B = -0.51$) were derived for the experimental geometry employed in Fig. 6. (C) Hypothetical H₂O spectra with OH bonds assumed decoupled. Dashed line corresponds to the *ssp* spectrum of 25% HDO isolated in D₂O ice (intermolecular coupling set to zero). (D) Fully coupled H₂O; the peak of the dangling-OH *ssp* feature is at 0.55 units.

has significant contributions from top three bilayers and is dominated by OH bonds which are oriented along the z axis and which connect the different bilayers. In the top bilayer, the net negative polarization in this frequency range is due to the fact that OH pointing in the $+z$ direction are dangling and correspond to much higher frequency of 3700 cm^{-1} . In the case of the second and third bilayers, the net polarization appears to be of a dynamic origin. Bonds pointing in the $-z$ direction (“into the ice slab”) are more tightly localized around the z axis than bonds pointing up (see Fig. 5, bottom). Not unexpectedly, the $\sim 3180\text{ cm}^{-1}$ peak dominates also the decoupled χ_{zzz} element, which favors the z -oriented bonds [blue curve in Fig. 4(A)]. Note that χ_{zzz} in Fig. 4(A) was reduced by a factor of 2 and thus its negative peak is much larger than that of χ_{yyz} ; however, the $\sim 3180\text{ cm}^{-1}$ peaks corresponding to the two polarizations strongly overlap.

Inclusion of intramolecular coupling only (as in H₂O isotopically isolated in D₂O) has a minor effect on the two χ elements (not shown), due to the smallness of the intramolecular coupling element in condensed phases, as discussed in Sec. II. On the other hand inclusion of the long range intermolecular dipole-dipole coupling has a significant effect on the susceptibility elements [compare panels (A) and (B) in Fig. 4]. In the coupled system, χ_{yyz} and χ_{zzz} line shapes differ substantially from each other. χ_{yyz} peaks at 3000 cm^{-1} , at the same frequency as the computed parallel-polarized Raman spectrum in Fig. 1(A). On the other hand, χ_{zzz} peaks at 3178 cm^{-1} , near the maximum of the computed IR spectrum. χ_{zzz} includes also a smaller subsidiary peak at 3000 cm^{-1} .

The nature of excitations contributing to χ_{yyz} and χ_{zzz} in the coupled system is of interest. It is noted that the intermolecular coupling results in significant broadening of the den-

sity of ice states with respect to the decoupled case [compare cyan and blue curves in Fig. 1(A)]. Moreover in the fully coupled H₂O-ice system the excited states correspond to collective modes delocalized over the entire system.⁴⁰ As dis-

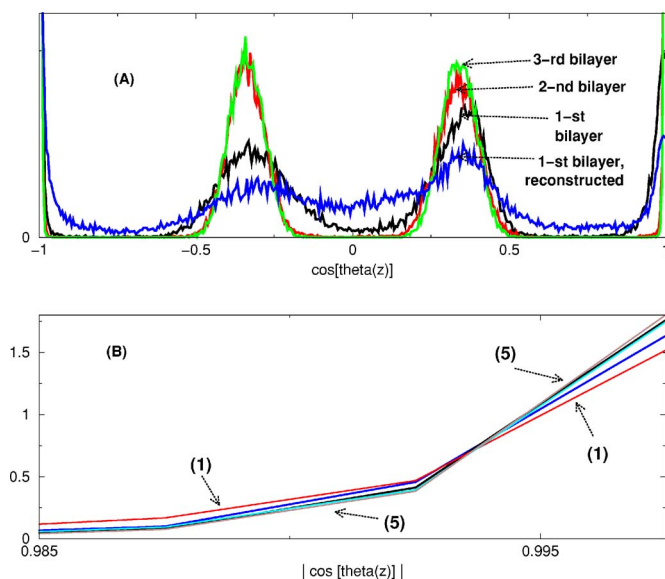


FIG. 5. (Color online) Distribution of $\cos[\theta(z)]$, where $\theta(z)$ denotes an angle of a OH bond with respect to the z axis. $\cos[\theta(z)]$ was averaged over 1 ps sections of classical trajectory; see Sec. II. Panel (A): distributions of $\cos[\theta(z)]$ for the first, second, and third bilayers of the crystal ice slab and for the reconstructed top bilayer, see end of Sec. III. Panel (B): distribution of $|\cos[\theta(z)]|$ for z -oriented OH bonds connecting the bilayers for the crystal slab model. From bottom to top on the right and from top to bottom on the left, the five lines correspond to (1) top bilayer, OH pointing down into the surface; (2) second bilayer, up; (3) second bilayer, down; (4) third bilayer, up; and (5) third bilayer, down.

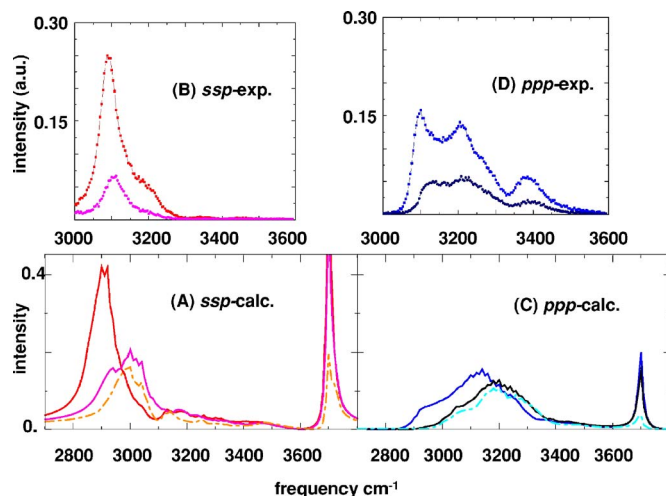


FIG. 6. (Color online) Computed spectra of crystal ice surface [(A) and (C)] compared to experimental ones in the H-bonded region [(B) and (D)]. The computed spectra correspond to the experimental geometry. Since the model overestimates OH frequency shift due to H bonding, the scales of the top and the bottom spectra were displaced with respect to each other, so that the computed and the experimental spectral bands roughly overlap. Dot-dashed lines in panels (A) and (C) correspond to an ice model with a partially reconstructed top bilayer, see text. Three ice bilayers were included in the calculations. The same relative units are used for all computed spectra. Panels (A) and (C): computed spectra in the order of decreasing peak intensities correspond to 128 K (crystal surface), 190 K (crystal surface), and 190 K (reconstructed surface). Panels (B) and (D): experimental spectra in the order of decreasing peak intensities correspond to 128 and 178 K.

cussed in the past,⁴⁰ the Raman and IR spectra of the coupled H₂O ice system differ substantially from each other and from the density of states [compare the different curves in Fig. 1(A)], since the two spectroscopic techniques excite preferentially different types of collective modes. The collective vibrations contributing the low frequency Raman peak were described as globally in-phase “breathing” modes.^{40,46,83} The higher frequency IR peak is due to excitations in which the molecular dipoles corresponding to asymmetric stretch oscillate in phase.^{40,83} Since the χ elements include both polarizability and dipole matrix elements, they can be considered as a kind of a convolution of Raman and infrared spectra, albeit weighted by the surface polarization. Thus the ice χ elements in Fig. 4(B) appear to be dominated by the same two types of collective modes as the Raman and IR spectra; i.e., χ_{yyz} and χ_{zzz} are dominated by Raman-active and IR-active modes, respectively. These modes acquire their SFG intensity from surface polarization.

Right panels [(C) and (D)] of Fig. 4 show the *ssp* and *ppp* spectra of ice, calculated for the decoupled and coupled cases, respectively. For the relative units used in the figure, $\chi_{\text{eff},ssp}^{(2)} = \chi_{yyz}$; $\chi_{\text{eff},ppp}^{(2)} = -0.70\chi_{xxz} + 0.36\chi_{zzz}$; the latter coefficients were derived for the experimental geometry used in Fig. 6. (See Introduction for further details on how the spectrum is obtained from the χ elements.) In the absence of coupling [panel (C)], the *ssp* spectrum would be dominated by a single peak at 3180 cm⁻¹. The *ppp* spectrum would peak at the same frequency due to similarity between χ_{zzz} and $\chi_{xxz}(=\chi_{yyz})$ line shapes in panel (A); however, the *ppp* intensity would be four times smaller than *ssp* due to destructive interference of the overlapping *xxz* and *zzz* compo-

nents. The intermolecular coupling redshifts the *ssp* spectrum by ~ 200 cm⁻¹ [panel (D)]. In contrast to the decoupled case, the coupled *ssp* and *ppp* spectra are displaced with respect to each other, since the overlap between χ_{zzz} and χ_{xxz} is reduced significantly [see panel (B)]. Moreover the *ssp* and *ppp* intensities are now comparable, due to reduced interference between the *xxz* and *zzz* components, although the *ppp* peak intensity is still smaller than that of *ssp*.

Note that the spectra shown in panel (C) would not correspond to HDO isotopically isolated in D₂O, because of the nonresonant contribution which does not diminish upon isotopic dilution. For 25% HDO, the *ssp* spectrum would correspond to a dashed line in panel (C).⁸⁴ Nevertheless, in an experimental study deconvolution of the nonresonant contribution might be possible, as was done in the case of the liquid.⁵⁴

Figure 6 shows the computed ice spectra versus the experimental ones for single crystal basal plane surfaces, for the *ssp* and *ppp* polarizations. Though the agreement is far from quantitative, several experimental features are qualitatively reproduced. These include the relatively sharp *ssp* peak appearing in the low frequency range of the Raman-active modes and the significant reduction of the intensity of this peak with increasing temperature. Similar to the experiment, the computed *ppp* spectra extend from the Raman-active to the IR-active higher frequency regime. However, in disagreement with experiment, the low frequency wing of the computed *ppp* spectra is less intense than the high frequency wing. At both temperatures, the peak intensity of *ppp* is smaller than that of *ssp*, in accord with experiment.

It is noted at this point that computation of the relative contributions of χ_{xxz} and χ_{zzz} to *ppp* spectra requires as input n' , the index of refraction of the interface layer at $\omega_{\text{vis}} \approx \omega_{\text{SFG}}$. The “best” value of n' has been a subject of considerable debate; see, e.g., Refs. 29 and 31, and references therein. In the present calculation of spectra, two choices were tried—one with n' equal to that of ice, and another with the average index of refraction of ice and vacuum; these choices are in the general range used in the past in the literature. The first choice yielded the spectra shown in Fig. 6. The second choice resulted in enhanced discrepancy with respect to experiment, as the computed intensity of the high frequency wing of the *ppp* spectrum became much larger (by a factor of ~ 2) than the *ssp* peak intensity. The use of the ice index of refraction for n' appears consistent with significant contribution from the subsurface to the SFG signal and with the fact that the pertinent OH-stretch excitations are delocalized over the ice sample.

A number of additional discrepancies are apparent in the computed spectra, with respect to experiment. The measured distinct small peak at 3400 cm⁻¹ is absent in the computed *ppp* spectra although a high frequency wing is calculated in this spectral region. The frequency shift between the 128 and 190 K spectra is overestimated, as is the frequency shift of the ice spectra with respect to the liquid spectra. These overestimated frequency shifts are most likely due to classical rather than quantum-mechanical treatment of intermolecular motion. The effect of intermolecular motion on the OH-stretch spectra is modeled via averaging of the electric field

at the H atom of OH over a section of a classical trajectory. Upon freezing of the liquid, and upon further cooling of the ice, the amplitude of the classical intermolecular motion decreases significantly, resulting in strengthening of H bonds and exaggerated frequency redshifts; in reality, reduction in intermolecular motion amplitude is mitigated by the quantum-mechanical zero-point motion.

Lack of zero-point motion may also account for overestimation of the *ssp* *d*-OH band intensity at 3700 cm^{-1} . In the present set of experimental data, detailed results on the *d*-OH band are not yet available. Preliminary results indicate much lower *d*-OH peak intensity than that of the H-bonded OH-band, in accord with past SFG studies of ice by Wei *et al.* in the 173–271 K range.⁷ For example, in the 173 K *ssp* spectrum of Fig. 7(A), *d*-OH peak intensity is an order of magnitude smaller than that of the H-bonded band. On the other hand, the computed *d*-OH peak intensity at 190 K is about three times larger. While accurate measurements of the *d*-OH band intensity are known to be difficult due to impurity problem, the computed value is most likely too large. The large computed *d*-OH intensity is due to the fact that in a crystal surface, *d*-OH bonds are aligned along the *z* direction, and classical thermal motion induces only modest angular delocalization (Fig. 5). Inclusion of zero-point angular delocalization is expected to reduce significantly the polarization of *d*-OH and the corresponding SFG intensity.

Surface reconstruction could be an additional factor affecting significantly the *d*-OH intensity as well as the H-bonded SFG band shape. A number of past computational studies (see, e.g., Refs. 41, 85, and 86) suggested that the top ice bilayer undergoes reconstruction to a disordered structure at some temperature below surface melting. Surface reconstruction was proposed to be associated with reduction of surface dangling atoms, increase in the number of four-coordinated surface molecules (albeit with a strained coordination shell), and appearance of a distribution of surface ring sizes instead of six-membered rings only, as in a perfect crystalline surface. While simulations indicate that reconstruction does not require much energy, the transition temperature obtained in simulations is not expected to be particularly reliable. Onset of disorder at about 2/3 of the ice melting point is expected. It is of interest to predict the effect of such surface disordering on the SFG spectra.

For this purpose, each of the ice models was subjected to a 5 ps classical trajectory at 275 K. (The temperature was rescaled to 275 K every 0.1 ps.) This run is used to induce prompt partial melting of the top bilayer. The slab was then recooled to 190 K and the SFG spectrum calculated as described in Sec. II. A surface snapshot of a partially reconstructed and a nonreconstructed surface bilayer at 190 K is shown in Fig. 7. The effect of reconstruction on the H-bonded SFG signal is surprisingly small, see dot-dashed lines in Fig. 6. This result is consistent with significant contribution to the signal from the ice subsurface. The main effect of reconstruction is substantial reduction of the *d*-OH band intensity in the *ssp* spectrum [see Figs. 6(A)–6(C)]. This is since surface disordering reduces the number of *d*-OH and broadens their orientational distribution (Fig. 5). Onset of reduction of the *d*-OH signal was, in fact, measured

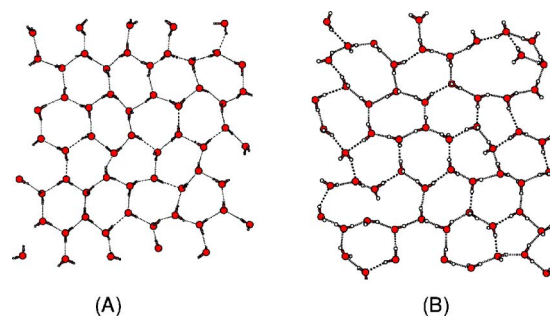


FIG. 7. (Color online) A snapshot of a crystal top bilayer of ice and of a partially reconstructed top bilayer from a 190 K simulation.

by Wei *et al.* at 200 K,⁷ well below the temperature expected for surface melting. Further heating resulted in continuous decrease of the *d*-OH signal, indicating progressive disordering with increasing temperature.

IV. RESULTS: LIQUID

In the discussion below, a liquid “layer” is defined to contain 60 molecules, the same number as an ice bilayer in the original ice slab, before melting. That is, water molecules are first sorted according to *z* value; the first 60 molecules are defined as the top layer, the next 60 molecules as the second layer, etc. A pair of water molecules is defined as H bonded, if a near-neighbor intermolecular O..H distance is less than 2.5 \AA . (This cutoff corresponds to a minimum after the first peak in the intermolecular O..H distance distribution for the EMP.)

Figure 8 shows the calculated χ elements in the H-bonded region of the liquid. In panels (A) and (AA) the coupling between OH bonds was turned off; panel (B) corresponds to a fully coupled H₂O. In accord with past theoretical studies of liquid H₂O spectra,^{33–38} the net polarization of the dominant H-bonded band is negative, i.e., “into the surface.” In the decoupled-OH case [panel (A)] χ_{yyz} and χ_{zzz} attain largest (negative) values at $\sim 3350\text{ cm}^{-1}$. Most of the signal originates from the top layer. Panel (AA) shows contributions to χ_{yyz} from the different water coordinations. It is seen that the largest single contribution to χ_{yyz} in the negative H-bonded region corresponds to the four-coordinated molecules. This contribution amounts to 61% of χ_{yyz} , integrated over the $3000\text{--}3490\text{ cm}^{-1}$ range. Additional contributions in this range include the “companion” H-bonded OH bonds of the three-coordinated *d*-H molecules (19%), three-coordinated *d*-O molecules (7%), and H-bonded OH of asymmetrically connected two-coordinated molecules (11%; the latter molecules form one H bond via H and another via O). One may note that the contribution of the four-coordinated molecules to χ_{yyz} displays significant positive polarization in the $3500\text{--}3600\text{ cm}^{-1}$ regime of weak hydrogen bonding; however, this contribution is largely canceled by the negative one of the three-coordinated molecules with dangling O, and the two-coordinated water molecules.

The fact that χ_{yyz} incorporates contributions from a range of coordinations is in qualitative accord with a recent study⁹ employing the computational scheme of Ref. 33 and the POL3 water potential; however, in that study, the single

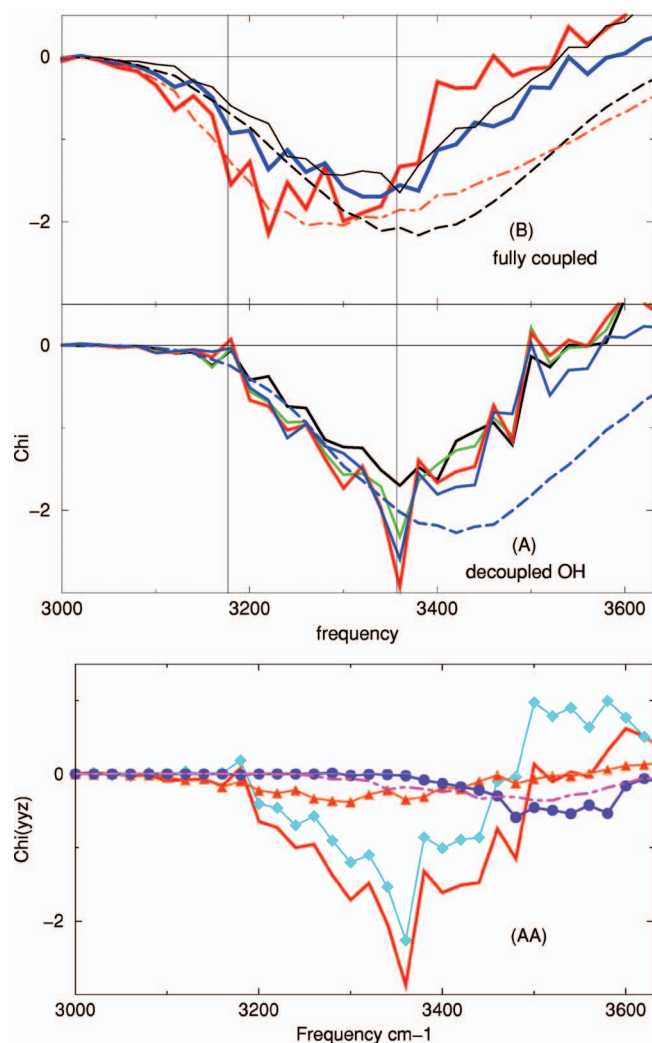


FIG. 8. (Color) Resonant contribution to χ elements for liquid water; the same relative units are used for all elements. (AA): decoupled OH bonds (“HDO isotopically isolated in D₂O”). Solid line corresponds to χ_{yyz} calculated with three-top layers of water. Other lines show contributions of H₂O of different hydrogen-bond coordinations to χ_{yyz} : Diamonds, OOH molecules (“two bonds via O, two bonds via H,” 61%); triangles, OOH (19%); circles, OHH (7%); and dot dashed, OH (11%). The numbers in parentheses denote integrated percent contributions to χ_{yyz} in the 3000–3490 cm⁻¹ range within the negative H-bonded band. (A) decoupled OH bonds. Solid black, green, and red lines correspond to χ_{yyz} calculated with one, two, and three top layers of water, respectively. The results for five layers are very similar to those for 3. Blue: χ_{zzz} , calculated with three layers, and reduced by a factor of 2 to ease the comparison with χ_{yyz} . Dashed line: density of (decoupled) states of the liquid [blue curve of Fig. 1(C)] multiplied by -1 to ease the comparison with χ elements. (B) Fully coupled H₂O. Color coding as in (A), except black and blue correspond to five liquid H₂O layers. Dashed and dot-dashed lines: calculated IR and parallel-polarized Raman spectra of liquid H₂O [black and red curves of Fig. 1(C)] multiplied by -1 to ease the comparison with the χ elements.

largest contribution to χ_{yyz} corresponded to the companion OH of the *d*-H molecules. The apparent reason for this difference is a different distribution of H₂O coordinations within the surface layer, for the EMP and POL3 potentials.

As seen in Fig. 8(A), the decoupled band shapes for $\chi_{yyz} = \chi_{xxz}$ and for χ_{zzz} are very similar to each other, as in the case of ice (compare the red and the blue curves). The negative susceptibility band extends roughly over the lower two-thirds of the density of frequencies; i.e., the polarization

originates from the relatively strongly H-bonded OH which tend to point preferentially into the ($-z$) direction and moreover correspond to enhanced bond dipole derivative.^{42,87} Reduced susceptibility at the high frequency end of the H-bonded density of frequencies is due to lack of net orientational preference for the corresponding weakly H-bonded OH, as noted above.

As in the case of ice, inclusion of intramolecular coupling has a minor effect on the χ elements (not shown). The effect of intermolecular coupling is much more substantial, resulting in significant broadening of χ_{yyz} towards low frequencies. χ_{yyz} corresponds now to a broad peak extending from ~ 3180 to ~ 3380 cm⁻¹. This peak overlaps roughly with the maximal intensity range of the bulk Raman spectrum; the high frequency end coincides with the peak of the IR spectrum.

As in the case of ice, the coupled χ_{zzz} peak overlaps with that of the IR spectrum. The overlap between the broad χ_{zzz} and χ_{yyz} bands is much more substantial than in the case of ice, resulting in significant interference effects in the *ppp* spectra, as discussed further below.

Properties of the vibrational excitations contributing to the liquid H₂O spectra are now considered. The intermolecular coupling results in delocalization of the OH excitations within the liquid, as already pointed out in past experimental^{46,50–52} and theoretical^{45,46} studies of liquid IR and Raman spectra. The experimental evidence for collective modes is the observed substantial difference between the Raman spectra of H₂O and of isotopically decoupled HDO, and between the IR and the parallel- and perpendicular-polarized Raman spectra of liquid H₂O (Refs. 46 and 50–52) [see Figs. 1(C) and 1(D)]. As in the case of ice, the differences originate from the fact that the IR and Raman intensities depend on relative phases of the bond vibrations in the collective modes, and the two spectroscopic techniques excite preferentially different types of such collective modes.

Some of the properties of the vibrationally excited states of liquid H₂O are displayed in Figs. 9 and 10; the different properties are defined in the figure captions. Maximum delocalization of the excited states is obtained at 3380 cm⁻¹, some 70 cm⁻¹ below the peak of the density of states [Fig. 9(A)]. The excited states at the OH-band edges tend to be localized on individual OH bonds. In the range corresponding to the broad negative χ_{yyz} peak shown in Fig. 8(B), the average extent of delocalization increases from ~ 3 to ~ 14 OH bonds as the frequency increases from 3200 to 3380 cm⁻¹. One may note that typically bonds contributing to an excited state *do not* belong to the same molecule [compare solid and dashed curves of Fig. 9(A)]. This is since intramolecular coupling in condensed H₂O is relatively small^{42,44} and moreover typically two bond frequencies belonging to the same H₂O molecule differ considerably from each other, due to differing strengths of H bonding; the mean intramolecular frequency difference between the two bonds is ~ 110 cm⁻¹. [The distribution of frequency differences is rather broad, see Fig. 10(B).] States in the 3200–3380 cm⁻¹ frequency range relevant to the SFG-*ssp* spectra are delocalized over relatively strongly H-bonded OH. Interestingly, inspection of system snapshots indicates that these bonds do

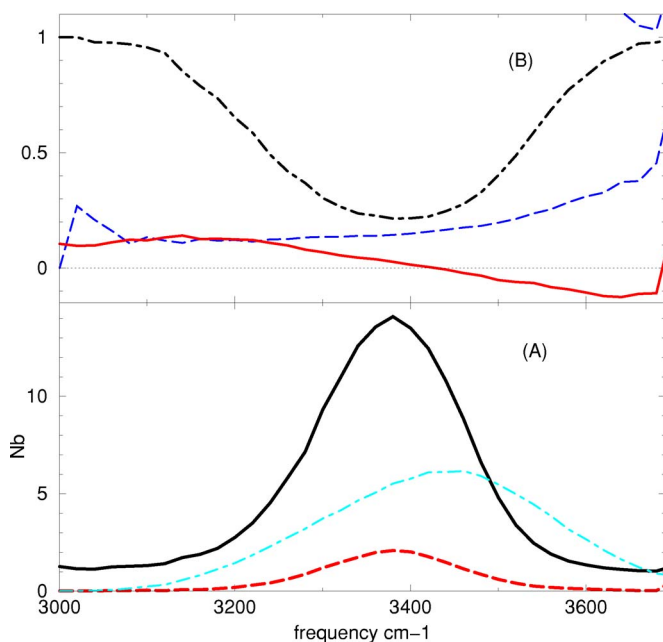


FIG. 9. (Color online) Excited state properties for the OH Hamiltonian corresponding to five layers of liquid H₂O. An excited state is expanded in the exciton basis localized on the different OH bonds $|\psi_{exc} = \sum_b c_b |1_b\rangle$. (A) Solid: N_b , average number of bonds contributing to an excited H₂O state in a liquid. N_b was calculated by (i) sorting bond expansion coefficients c_b according to their absolute value and (b) adding $|c_b|^2$ in decreasing order until the sum exceeded 0.6. N_b is the number of terms contributing to the sum. Dashed: Average number of OH for which both OH bonds of a molecule contribute to the sum. Dot-dashed: density of states. (B) Solid: average ratio of coefficients c_b for pairs of bonds belonging to the same molecule; measures local molecular symmetry of the states. Dot-dashed: global symmetry parameter defined as $S = [\sum_b |c_b|] / N_b$; the sum is over N_b most-significantly contributing states. $S=1$ for a globally symmetric state with all c_b having the same sign. $S=0$ corresponds to an equal number of positive and negative contributions. Dashed: fractional contribution of the top layer to an excited state. The averages are over excited states within 20 cm⁻¹ wide frequency bands.

not necessarily form continuous H-bonded chains. Significant mixing occurs between oscillations of bonds which happen to be in resonance with each other, and such mixing is possible over some distance, due to the long range nature of the dipole-dipole coupling. While in liquid the extent of delocalization is greatly reduced with respect to ice (from the entire system to several OH bonds), the low frequency portion of the OH frequency band still corresponds to collective in-phase “breathing-type” vibrations. It is seen in Fig. 9(B) that the low frequency liquid H₂O excitations retain some globally symmetric character, which decreases as the frequency increases. One may note finally that despite the low intramolecular coupling, the states below 3440 cm⁻¹ retain, on the average, weak local symmetric-stretch character, while the states above 3440 cm⁻¹ have weak antisymmetric-stretch character. [That is, the average ratio c_b/c_{b+1} between contributions of two bonds of a molecule to an excited state is a small positive/negative number in the two frequency regimes, see solid curve in Fig. 9(B). The latter result is qualitatively consistent with the results of Ref. 33, which, however, employed a much larger intramolecular coupling constant.]

Figure 11 shows the computed *ssp* and *ppp* spectra of

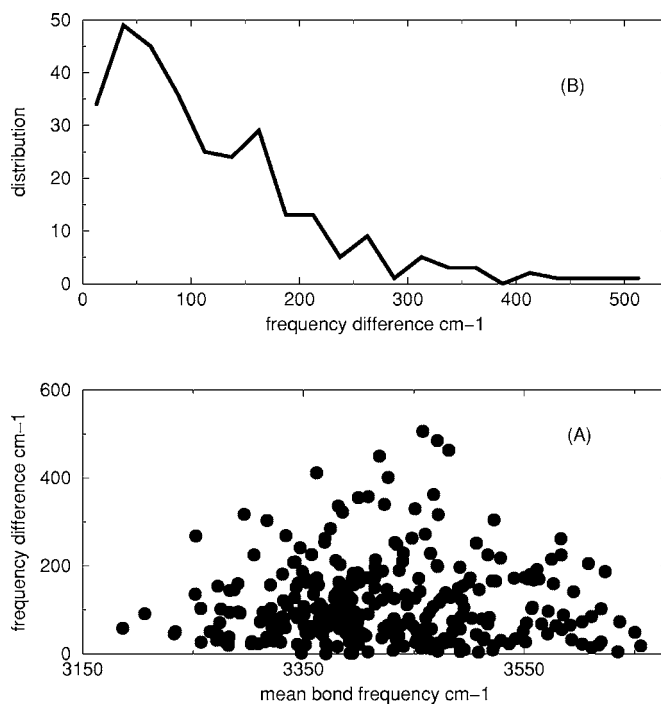


FIG. 10. Bond-frequency properties for one of the liquid configurations contributing to the spectra; five liquid layers were included. (A) Difference between two bond frequencies of a molecule vs the average bond frequency. (B) Distribution of differences between two bond frequencies of a molecule.

the neat water surface as a function of the visible beam incidence angle β_{vis} ; the computed results are compared to the experimental spectra of Gan *et al.*¹⁰ In the calculation of the relative contributions of χ_{xxz} and χ_{zzz} to the *ppp* spectrum, the index of refraction of the interface was taken as the av-

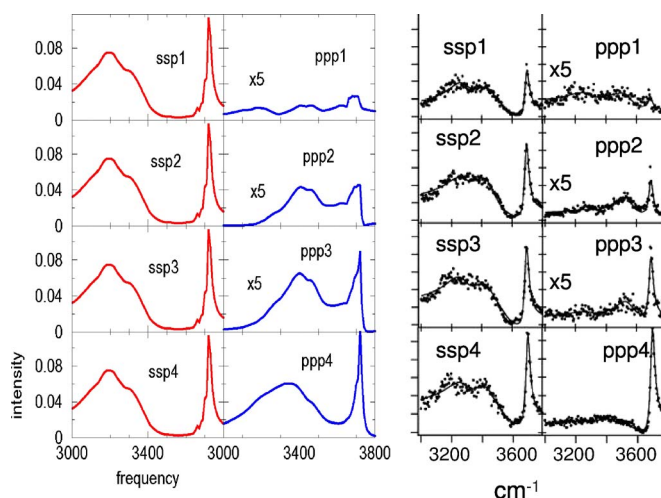


FIG. 11. (Color online) Left two columns: computed SFG spectra for liquid H₂O surface; same relative units are used for all the spectra. Five liquid layers were included in the calculation. Right two columns: experimental spectra of Gan *et al.* (Ref. 10) for different incident angles β_{vis} of visible radiation. β_{vis} values, from top to bottom, for both the experimental and the computed spectra: 39°, 45°, 48°, and 63°. Each pair of *ssp* and *ppp* spectra was multiplied by the same β_{vis} -dependent factor to eliminate the dependence of *ssp* spectra on incident angle. SFG-*ssp* spectrum is determined by χ_{yyz} and *ppp* spectrum is determined by a linear combination of $B\chi_{xxz} + C\chi_{zzz}$; the relative contributions (C/B) depend on the outgoing angle of the SFG beam β_{SF} , to a good approximation (Ref. 29) used in this computation, $\beta_{SF} \approx \beta_{vis}$.

erage of liquid water and vacuum.^{29,88} The computational model reproduces qualitatively the most dramatic finding—the very substantial reduction of the *ppp* intensity of the *d*-OH peak with the decreasing β_{vis} . Experimentally, the reduction is by a factor of 85, as compared to the computed value of 26. This result is due to nearly perfect cancellation of χ_{xxz} and χ_{zzz} contributions to $\chi_{\text{eff},ppp}^{(2)}$ at the smallest incidence angle. Moreover, for the two middle spectra corresponding to $\beta_{\text{vis}}=45^\circ, 48^\circ$ the calculation reproduces qualitatively the blueshift of the H-bonded *ppp* band with respect to *ssp*. The blueshift is due to cancellation of χ_{xxz} and χ_{zzz} components at the low frequency end of the *ppp* spectrum. Note that the negative peak of χ_{zzz} in Fig. 8(B) extends to higher frequencies than the negative peak in $\chi_{yyz}=\chi_{xxz}$.

Comparison between the computed and the measured *ssp* liquid spectra was already discussed in the end of Sec. II. As noted there, the main discrepancy appears to be missing intensity in the 3400–3500 cm^{-1} range. The effects of coupling on the vibrational spectra are usually assessed by comparing the OH band of a dilute solution of HDO in D_2O to the spectrum of neat H_2O . However, as noted in the previous section, in the case of SFG the measurement of the dilute HDO spectra is complicated by the fact that the nonresonant contribution does not diminish upon isotopic dilution⁵⁴ [see dashed spectrum for 25% HDO in D_2O ice, Fig. 4(C)]. Nevertheless, the pertinent experimental studies were carried out for liquid water by Raymond *et al.*⁵⁴ In that study, the resonant contribution to the spectrum was estimated while assuming several overlapping contributions to $\chi_{\text{eff},ssp}^{(2)}$ and fitting their parameters to the observed SFG signal. The top panel of Fig. 12 shows $|\chi_{yyz,R\Gamma}|^2$ derived from experiment, for 25% HDO in D_2O , and for H_2O . In order to compare HDO and H_2O line shapes in the H-bonded region, both line shapes were renormalized to correspond to the same integrated intensity in this region (to the red from the *d*-OH feature). The bottom panel of Fig. 12 shows calculated $|\chi_{yyz,R\Gamma}|^2$ for the fully coupled model and for the decoupled one; in the absence of the nonresonant contribution, the latter curve approximates dilute HDO. Comparison of the decoupled calculation to the HDO result derived from experiment is not entirely straightforward, since at the experimental 25% concentration the coupling effects may still be significant. Moreover the line shape derived from the experiment may depend on the functional form used in the fit. On the other hand the computed spectra depend on the assumed Lorentzian form used to model damping (see Sec. II). Nevertheless both the computed spectra and the spectra derived from experiment display intensity enhancement for H_2O with respect to HDO in the low frequency end of the spectrum.

(One may note enhancement by about a factor of 1.6, of the *d*-OH peak in the renormalized experimental HDO spectrum, with respect to H_2O . This factor corresponds to enhancement of the *d*-OH population by about 26%. Part of this enhancement can be accounted for the preference of single donor HDO to bond via D rather than via H, which has been documented in the past for clusters⁸⁹ and for ice surfaces.⁹⁰ This quantum-mechanical effect is due to zero-point energy differences; the energetic preference was estimated as $\Delta E=52\pm 8 \text{ cm}^{-1}$ for ice and $\sim 60 \text{ cm}^{-1}$ for clusters.

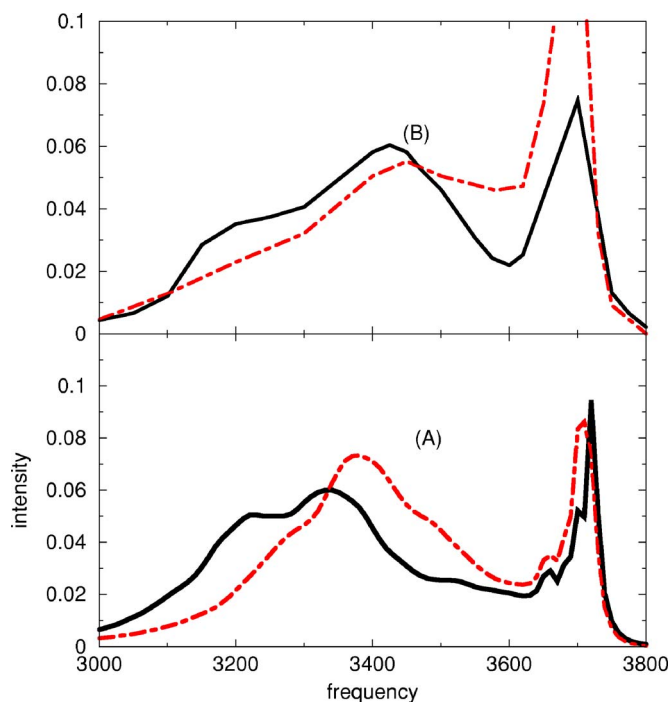


FIG. 12. (Color online) (A) Computed squared resonant contribution to the liquid H_2O *ssp* spectrum $|\chi_{yyz,R\Gamma}|^2$. Five liquid layers were included in the calculation. Dot-dashed, OH bonds assumed decoupled and solid, fully coupled H_2O model. (B) $|\chi_{yyz,R\Gamma}|^2$, derived from experiment, adopted from Figs. 2 and 4 of Ref. 54. Solid, H_2O and dot-dashed, 25% HDO isolated in D_2O . In both panels, in order to compare HDO and H_2O line shapes in the H-bonded region, both line shapes were renormalized to correspond to the same integrated intensity in this region (to the red from the *d*-OH feature). The spectra in the top and bottom panels are given in (different) relative units.

Using the larger 60 cm^{-1} value one obtains *d*-OH enhancement by 14%, about half of the observed value. Additional contribution to the *d*-OH SFG peak enhancement in HDO with respect to H_2O may originate from enhanced local mode character of *d*-OH in dilute HDO.)

V. RESULTS: A SLAB WITH A SINGLE ION

As described in the end of Sec. II, the effect of acid on the SFG spectrum was modeled by adding a single hydronium ion to the system. For the potential parameters chosen, the ion spent most of the 2500 ps trajectory at one of the slab surfaces, which was then used to calculate the SFG spectrum. The inset to Fig. 13 shows a typical surface configuration of H_3O^+ and its three near-neighbor water molecules.

Figure 13 shows comparison between the SFG-*ssp* spectra of the water slab with and without the hydronium ion. For comparison, experimental spectra of HCl solution at $\text{pH}=0.5$ and 0.1 are displayed (from Ref. 21). The calculation reproduces qualitatively the amplification of the H-bonded OH-stretch band in the *ssp* spectrum by protonated water at the surface, although it fails to reproduce the asymmetry of the enhanced band, with excess intensity at the low frequency end. The amplification is due to hydronium orienting the water molecules within the solvation shell. Comparison of orientational properties at the surface, with and without the hydronium, is displayed in Fig. 14. It is seen that the distribution of water bisector orientations is enhanced to-

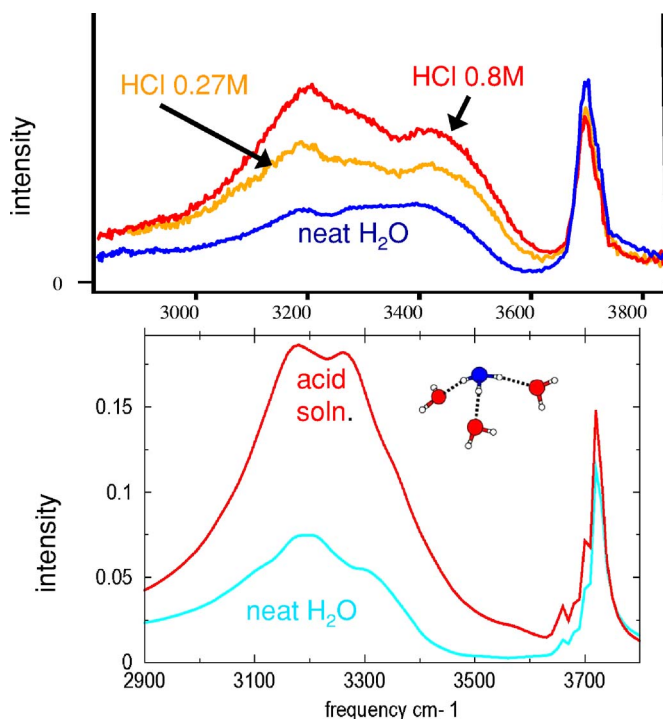


FIG. 13. (Color online) Bottom: computed SFG-ssp spectra for neat H_2O and for an acid solution model with a single H_3O^+ ion at the liquid H_2O surface. Same relative units are used for both spectra. Five liquid layers were included in the calculation. Top: experimental ssp spectra of the neat vapor/water interface and the vapor/HCl solution interface at 0.27 and 0.8M (pH 0.5 and 0.1), respectively, from Ref. 21.

wards negative $\cos(\theta)$, i.e., bisectors pointing into the surface; see diamonds, Fig. 14(C). [In addition, there is some enhancement towards water planes being parallel rather than perpendicular to the liquid surface, see triangles in Fig. 14(C).]

The comparison between computation and experiment is not straightforward. In the experimental system, both hydronium and chloride ions are present. Chloride ions do not display strong surface preference, as indicated by a small effect of NaCl solute on SFG spectra in the pertinent concentration range.⁵ However, formation of an electrical double layer at the surface in the presence of both ions may have a significant effect on the spectra.^{2,38} Moreover it is difficult to compare the computed and experimental concentration scales. One acid molecule per 600 water molecules corresponds to the experimental concentration of 0.1M. However, the choice of the present potential parameters (see end of Sec. II), in addition to the use of a single cation in the model, may exaggerate the surface propensity of the proton with respect to experiment, resulting in the overestimation of the acid effect on the H-bonded region. Nevertheless, the observed major amplification of the SFG signal in the H-bonded region appears to be accounted for by the orienting effect of the hydronium ions on the surrounding water molecules.

In the *d*-OH region, the calculation indicates modest amplification of the peak signal, while the experiment shows modest reduction.^{21,91,92} The calculated amplification appears

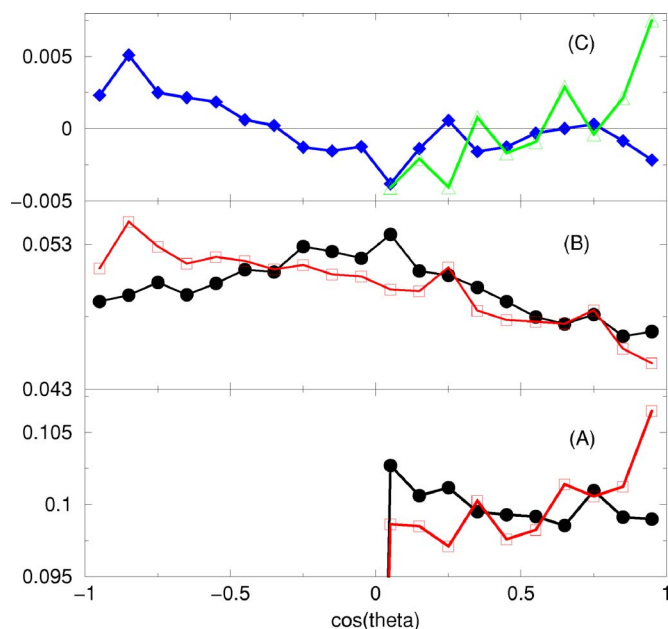


FIG. 14. (Color online) [(A) and (B)] Molecular angular distributions corresponding to the top five liquid water layers with (squares) and without (circles) H_3O^+ at the surface. (A) Distribution of cosines of angles between H_2O normals to molecular planes and the z axis. (B) Distribution of cosines of angles between the water bisector and the z axis. (C) Diamonds: the difference between the two curves in (B)—the curve demonstrates excess molecules with bisectors pointing “into the surface.” Triangles: the difference between the two curves in (A).

to be due to the increase of surface roughness in the presence of the ion; the effect may be exaggerated by the limited size of the model.

VI. SUMMARY

An exciton-based computational model was developed for calculation of SFG spectra of water-containing systems in the OH-stretch region. The advantages of the present scheme are quantum-mechanical treatment of OH-stretch degrees of freedom and relative ease of interpretation as the properties of the excited states contributing to the spectrum can be assessed by analyzing the contributions of the different OH bonds to the vibrational wave functions. The intermolecular degrees of freedom are treated classically. The influence of H bonds on OH-stretch frequencies is modeled via average electric field E at the H atom of a OH bond; the bond frequency is assumed to be a function of mean E value, averaged over intermolecular motion. Both inter- and intramolecular coupling effects are included. The effect of the latter is modest, due to the smallness of the corresponding coupling constant in condensed phases.^{44,55} On the other hand, inclusion of the long range intermolecular (dipole-dipole) coupling is crucial for the interpretation of ice SFG spectra, and has significant effect on the liquid spectra as well. In ice, vibrational excitations are collective, and spectroscopic response depends on relative phases of different OH bonds in the extended excited states. In the liquid, more modest delocalization was obtained; the excitations extend typically over several OH bonds which happen to be in resonance with each other and which typically belong to different molecules.

The present calculations reproduce and provide an interpretation for a number of qualitative features in the experimental spectra of the surfaces of ice, liquid, and acid solutions. In ice, the Raman-active globally symmetric modes are major contributors to the χ_{yyz} susceptibility, and thus dominate the *ssp* spectrum. These modes contribute also to the low frequency end of the ice *ppp* spectra, while the high frequency part of the main *ppp* feature is assigned to the IR active in-phase dipolar modes, and originates from χ_{zzz} . The ice surface polarization is dominated by OH bonds connecting the top three ice bilayers. Subsurface polarization is of dynamic origin. Specifically, in the second and third bilayers, the bonds pointing down are localized more tightly around the surface normal than the bonds pointing up, resulting in the net polarization. The computations on ice reproduced qualitatively the measured dramatic increase in the H-bonded *ssp*-band intensity observed upon lowering of the temperature. In addition to the ordered basal plane ice surface, reconstructed partially disordered ice surface was considered. This is since disordering of the top ice bilayer was suggested in the past to take place well below the surface melting point.^{41,85,86} Such surface reconstruction is shown to affect predominantly the *d*-OH band of the SFG spectrum. Onset of reduction of the *d*-OH signal was, in fact, measured in the past for the ice surface above 200 K.⁷

In the case of liquid H₂O, polarization in the H-bonded region is dominated by OH which form relatively strong hydrogen bonds in the top surface layer; polarization is due to the fact that such OH tend to point preferentially into the surface. Intermolecular coupling results in broadening of the resonant contribution to the H-bonded band towards low frequencies, in accord with the experimental isotopic dilution studies of Ref. 54. The computation reproduced qualitatively the evolution of the liquid *ppp* spectra as a function of incident angle of the visible beam, as measured by Gan *et al.*;¹⁰ the evolution is due to interference effects between χ_{xxz} and χ_{zzz} susceptibility elements.

Finally, initial effort was made to reproduce the observed effect of acid solute on the H-bonded OH-stretch band in the liquid *ssp* SFG spectrum.^{2,6,19–21} While the current computational model is certainly oversimplified, it reproduces qualitatively the observed amplification of the SFG spectrum in the H-bonded region. The amplification is due to the cation orienting H₂O bisectors into the surface within the solvation shell.

The agreement between the computed and experimental spectra is far from quantitative. The approximations include classical treatment of intermolecular motion and neglect of the Zundel-type ion contribution to the protonated-water dynamics. Perhaps the most significant limitation is the quasistatic treatment of the liquid spectra. The spectra were calculated as a sum of contributions from numerous liquid H-bond network configurations, for which the average OH-stretch Hamiltonian matrix was constructed and diagonalized. The OH-Hamiltonian parameters were averaged over 1 ps sections of a classical trajectory (since the lifetime of the H-bond network in the liquid is of order of 1 ps). In reality, the H-bond network of the liquid evolves continu-

ously, modulating the OH vibrations. Work is in progress to take into account this continuous modulation in the calculation of the spectra.

The main discrepancy between the computation and the experiment is missing intensity in the high frequency end of the H-bonded part of the computed spectra. In the case of the liquid, the computed spectrum decreases rather abruptly in the 3340–3420 cm⁻¹ range, as compared to the experimental spectrum which decays more gradually in the 3400–3600 cm⁻¹ range. In the case of the ice, the computation did not reproduce a small but distinct peak at 3400 cm⁻¹ observed in the measured *ppp* spectrum. These discrepancies may be related to neglect of the coupling of OH stretch to the bending overtone, which is likely to affect this spectral region.⁹³ Alternatively (or additionally) some of the intensity in this region, as well as the observed broad bands in the vicinity of the dangling-OH feature,¹² may originate from combined excitations of OH stretch with intermolecular modes; such excitations are not included in the present model.

Note added in proof: Recently we became aware of calculations of SFG spectra for HCl and HI solutions by Ishiyama and Morita.⁹⁴

ACKNOWLEDGMENTS

The Israel Science Foundation is acknowledged for support by V.B., M.J.S., H.G., and I.L. acknowledge partial support of this work from the U.S. National Science Foundation, Grant No. CHE0240172. V.B. gratefully acknowledges helpful discussions with Hong Fei Wang, Paolo Miranda, Paul Devlin, Audrey Hammerich, Dave Walker, and Dennis Hore.

- ¹Y. R. Shen and V. Ostroverkhov, Chem. Rev. (Washington, D.C.) **106**, 1140 (2006); **103**, 3292 (1999).
- ²M. J. Shultz, C. Schnitzer, D. Simonelli, and S. Baldelli, Int. Rev. Phys. Chem. **19**, 123 (2000).
- ³M. J. Shultz, S. Baldelli, C. Schnitzer, and D. Simonelli, J. Phys. Chem. B **106**, 5315 (2002).
- ⁴G. L. Richmond, Annu. Rev. Phys. Chem. **52**, 357 (2001).
- ⁵D. Liu, G. Ma, L. M. Levering, and H. C. Allen, J. Phys. Chem. **108**, 2252 (2003).
- ⁶M. Mucha, T. Frigato, L. M. Levering, H. C. Allen, D. Tobias, L. X. Dang, and P. Jungwirth, J. Phys. Chem. B **109**, 7617 (2005).
- ⁷(a) X. Wei, P. B. Miranda, C. Zhang, and Y. R. Shen, Phys. Rev. B **66**, 085401 (2002); (b) X. Wei, P. B. Miranda, and Y. R. Shen, Phys. Rev. Lett. **86**, 1554 (2001).
- ⁸H. Groenzin, I. Li, and M. J. Shultz, *Physics and Chemistry of Ice*, edited by W. H. Kuhs (RSC Publishing, Cambridge, 2007), 191–199.
- ⁹D. S. Walker, D. K. Hore, and G. L. Richmond, J. Phys. Chem. B **110**, 20451 (2006).
- ¹⁰W. Gan, D. Wu, Z. Zhang, R. Feng, and H. Wang, J. Chem. Phys. **124**, 114705 (2006).
- ¹¹S. Baldelli, C. Schnitzer, M. J. Shultz, and D. Campbell, J. Phys. Chem. B **101**, 4607 (1997).
- ¹²D. Simonelli, S. Baldelli, and M. J. Shultz, Chem. Phys. Lett. **298**, 400 (1998).
- ¹³T. M. Chang and L. X. Dang, Chem. Rev. (Washington, D.C.) **106**, 1305 (2006).
- ¹⁴I. Benjamin, Acc. Chem. Res. **28**, 233 (1995); Chem. Rev. (Washington, D.C.) **106**, 1212 (2006).
- ¹⁵P. Jungwirth and D. J. Tobias, Chem. Rev. (Washington, D.C.) **106**, 1259 (2006).
- ¹⁶C. J. Mundy and I. F. W. Kuo, Chem. Rev. (Washington, D.C.) **106**, 1282 (2006).
- ¹⁷S. S. Iyengar, T. J. F. Day, and G. A. Voth, Int. J. Mass. Spectrom. **241**,

- 197 (2005).
- ¹⁸M. K. Peterson, S. S. Iyengar, T. J. F. Day, and G. A. Voth, *J. Phys. Chem. B* **108**, 14804 (2004).
- ¹⁹S. Baldelli, C. Schnitzer, and M. J. Shultz, *J. Phys. Chem. B* **101**, 10435 (1997).
- ²⁰C. Raduge, V. Pflumio, and Y. R. Shen, *Chem. Phys. Lett.* **274**, 140 (1997).
- ²¹T. L. Tarbuck, S. T. Ota, and G. L. Richmond, *J. Am. Chem. Soc.* **128**, 14519 (2006).
- ²²I. Kusaka and D. W. Oxtoby, *J. Chem. Phys.* **113**, 10100 (2000); *J. H. Seinfeld, Science* **288**, 5464 (2000).
- ²³J. W. Shin, N. I. Hammer, E. G. Diken, M. A. Johnson, R. S. Walters, T. D. Jaeger, M. A. Duncan, R. A. Christie, and K. D. Jordan, *Science* **304**, 1137 (2004).
- ²⁴C. C. Wu, K. C. Lin, H. C. Chang, J. C. Jiang, K. L. Kuo, and M. L. Klein, *J. Chem. Phys.* **122**, 074315 (2005).
- ²⁵S. S. Iyengar, M. K. Petersen, T. J. F. Day, C. J. Burnham, V. E. Teiqe, and G. A. Voth, *J. Chem. Phys.* **123**, 084309 (2005).
- ²⁶P. B. Petersen and R. J. Saykally, *J. Phys. Chem. B* **109**, 7976 (2005).
- ²⁷Y. R. Shen, *The Principles of Nonlinear Optics* (Wiley, New York, 1984), Chaps. 6 and 25.
- ²⁸C. D. Bain, *J. Chem. Soc., Faraday Trans.* **91**, 1281 (1995).
- ²⁹H. F. Wang, W. Gan, R. Lu, Y. Rao, and B. Wu, *Int. Rev. Phys. Chem.* **24**, 191 (2005).
- ³⁰C. Hirose, N. Akamatsu, and K. Domen, *J. Chem. Phys.* **96**, 997 (1992).
- ³¹X. Zhuang, P. B. Miranda, D. Kim, and Y. R. Shen, *Phys. Rev. B* **59**, 12362 (1999).
- ³²M. J. Shultz, "Sum frequency generation: An introduction plus recent developments and current issues," in *Progress in Multiphoton Proc. Spec.*, edited by S. H. Lin, A. A. Villaeys, and Y. Fujimura (World Scientific, Singapore, 2007, 17), in press.
- ³³A. Morita and J. T. Hynes, *Chem. Phys.* **258**, 371 (2000).
- ³⁴A. Morita and J. T. Hynes, *J. Phys. Chem. B* **106**, 673 (2002).
- ³⁵A. Perry, C. Neipert, C. R. Kasprzyk, T. Green, B. Space, and P. B. Moore, *J. Chem. Phys.* **123**, 144705 (2005).
- ³⁶A. Perry, C. Neipert, and B. Space, *Chem. Rev. (Washington, D.C.)* **106**, 1234 (2006).
- ³⁷A. Morita, *J. Phys. Chem. B* **110**, 3158 (2006).
- ³⁸E. C. Brown, M. Mucha, P. Jungwirth, and D. J. Tobias, *J. Phys. Chem. B* **109**, 7934 (2005).
- ³⁹T. Ishiyama and A. Morita, *Chem. Phys. Lett.* **431**, 78 (2006); *J. Phys. Chem. C* **111**, 738 (2007).
- ⁴⁰V. Buch and J. P. Devlin, *J. Chem. Phys.* **110**, 3437 (1999).
- ⁴¹B. Rowland, N. S. Kadagathur, J. P. Devlin, V. Buch, T. Feldman, and M. J. Wojcik, *J. Chem. Phys.* **102**, 8328 (1995).
- ⁴²V. Buch, S. Bauerecker, J. P. Devlin, U. Buck, and J. K. Kazimirski, *Int. Rev. Phys. Chem.* **23**, 375 (2004).
- ⁴³U. Buck, I. Ettischer, M. Melzer, V. Buch, and J. Sadlej, *Phys. Rev. Lett.* **80**, 2578 (1998).
- ⁴⁴J. Sadlej, V. Buch, J. K. Kazimirski, and U. Buck, *J. Phys. Chem. A* **103**, 4933 (1999).
- ⁴⁵V. Buch, *J. Phys. Chem. B* **109**, 17771 (2005).
- ⁴⁶S. A. Rice, M. S. Bergen, and A. C. Belch, *J. Phys. Chem.* **87**, 4295 (1983); M. S. Bergen and S. A. Rice, *J. Chem. Phys.* **77**, 583 (1982).
- ⁴⁷J. R. Reimers and R. O. Watts, *Chem. Phys.* **91**, 201 (1984).
- ⁴⁸S. A. Corcelli, C. P. Lawrence, and J. L. Skinner, *J. Chem. Phys.* **120**, 8107 (2004).
- ⁴⁹S. A. Corcelli and J. L. Skinner, *J. Phys. Chem. A* **109**, 6154 (2005).
- ⁵⁰D. E. Hare and C. M. Sorenson, *J. Chem. Phys.* **96**, 13 (1992).
- ⁵¹J. L. Green, A. R. Lacey, and M. G. Sceats, *J. Phys. Chem.* **90**, 3958 (1986).
- ⁵²S. Kint and J. R. Scherer, *J. Chem. Phys.* **69**, 1429 (1978).
- ⁵³H. Torii, *J. Phys. Chem. A* **110**, 9469 (2006).
- ⁵⁴E. A. Raymond, T. L. Tarbuck, and G. L. Richmond, *J. Phys. Chem. B* **106**, 2817 (2002).
- ⁵⁵J. P. Devlin, *Int. J. Radiat. Phys. Chem.* **9**, 29 (1990).
- ⁵⁶E. Whalley and D. D. Klug, *J. Chem. Phys.* **84**, 78 (1986).
- ⁵⁷V. Buch, P. Sandler, and J. Sadlej, *J. Phys. Chem. B* **102**, 8641 (1998); the EMP is denoted in this reference as "modified Kuwajima-Warshel potential;" the pertinent Kuwajima-Warshel article is referenced below.
- ⁵⁸S. Kuwajima and A. Warshel, *J. Phys. Chem.* **94**, 460 (1990).
- ⁵⁹J. Brudermann, U. Buck, and V. Buch, *J. Phys. Chem. A* **106**, 453 (2002).
- ⁶⁰J. P. Ryckaert, G. Cicotti, and H. J. C. Berendsen, *J. Comput. Phys.* **23**, 327 (1977).
- ⁶¹V. F. Petrenko and R. W. Whitworth, *Physics of Ice* (Oxford University Press, New York, 1999).
- ⁶²Q. Du, R. Superfine, E. Freysz, and Y. R. Shen, *Phys. Rev. Lett.* **70**, 2313 (1993).
- ⁶³J. R. Scherer and R. G. Snyder, *J. Chem. Phys.* **67**, 4794 (1977).
- ⁶⁴J. R. Scherer, M. K. Go, and S. Kint, *J. Phys. Chem.* **78**, 1304 (1974).
- ⁶⁵A. C. Belch and S. A. Rice, *J. Chem. Phys.* **78**, 4817 (1983).
- ⁶⁶L. Ojamae, J. Tegenfeldt, and K. Hermansson, *Chem. Phys. Lett.* **195**, 97 (1992).
- ⁶⁷M. J. Wojcik, V. Buch, and J. P. Devlin, *J. Chem. Phys.* **99**, 2332 (1993).
- ⁶⁸M. L. Sage, *Chem. Phys.* **35**, 375 (1978).
- ⁶⁹J. E. Bertie, B. F. Francis, and J. R. Scherer, *J. Chem. Phys.* **73**, 6352 (1980).
- ⁷⁰W. F. Murphy, *Mol. Phys.* **36**, 727 (1978).
- ⁷¹S. Ashihara, N. Huse, A. Espagne, E. T. J. Nibbering, and T. Elsaesser, *J. Phys. Chem. A* **111**, 743 (2007).
- ⁷²J. W. Caldwell and P. A. Kollman, *J. Phys. Chem.* **99**, 6208 (1995).
- ⁷³V. Buch, A. Milet, R. Vacha, P. Jungwirth, and J. P. Devlin, *Proc. Natl. Acad. Sci. U.S.A.* **104**, 7342 (2007).
- ⁷⁴R. Vacha, V. Buch, A. Milet, J. P. Devlin, and P. Jungwirth, *Phys. Chem. Chem. Phys.* **9**, 4736 (2007).
- ⁷⁵H. D. Downing and D. Williams, *J. Phys. Chem.* **80**, 1640 (1976).
- ⁷⁶M. E. Tuckerman, K. Laasonen, M. Sprik, and M. Parrinello, *J. Phys.: Condens. Matter* **6**, 93 (1994).
- ⁷⁷D. Marx, *ChemPhysChem* **7**, 1848 (2006).
- ⁷⁸V. Buch, A. Dubrovkiy, F. Mohamed, M. Parrinello, J. Sadlej, A. D. Hammerich, and J. P. Devlin, "HCl hydrates as model systems for protonated water," *J. Phys. Chem. A* (submitted).
- ⁷⁹K. Kim, K. D. Jordan, and T. S. Zwier, *J. Am. Chem. Soc.* **116**, 11568 (1994).
- ⁸⁰R. Knochenmuss and S. J. Leutwyler, *J. Chem. Phys.* **96**, 5233 (1992).
- ⁸¹D. J. Anick, *J. Mol. Struct.: THEOCHEM* **587**, 97 (2002).
- ⁸²G. S. Fanourgakis, E. Apra, W. A. de Jong, and S. S. Xantheas, *J. Chem. Phys.* **122**, 134304 (2005).
- ⁸³E. Whalley, *Can. J. Chem.* **55**, 3429 (1977).
- ⁸⁴In a more accurate calculation of the 25% HDO/75% D₂O spectrum, one should include intermolecular coupling. This is since on the average each HDO molecule has one HDO nearest neighbor, so OH...OH coupling effects are likely to be non-negligible.
- ⁸⁵G. J. de Kroes, *Surf. Sci.* **275**, 365 (1992).
- ⁸⁶K. Bolton and J. B. C. Pettersson, *J. Phys. Chem. B* **104**, 1590 (2000).
- ⁸⁷E. Whalley and D. D. Klug, *J. Chem. Phys.* **84**, 78 (1986).
- ⁸⁸P. X. Ye and Y. R. Shen, *Phys. Rev. B* **28**, 4288 (1983).
- ⁸⁹A. Engdahl and B. Nelander, *J. Chem. Phys.* **86**, 1819 (1987).
- ⁹⁰J. P. Devlin, *J. Chem. Phys.* **112**, 5527 (2000).
- ⁹¹C. Schnitzer, S. Baldelli, and M. J. Shultz, *J. Phys. Chem. B* **104**, 585 (2000).
- ⁹²S. Baldelli, C. Schnitzer, and M. J. Shultz, *Chem. Phys. Lett.* **302**, 157 (1999).
- ⁹³J. P. Devlin, J. Sadlej, and V. Buch, *J. Phys. Chem. A* **105**, 974 (2001).
- ⁹⁴T. Ishiyama and A. Morita, *J. Phys. Chem. A* **111**, 9277 (2007).